# Strong Light-Matter Interactions in Heterostructures of Atomically Thin Films

L. Britnell,[1] R. M. Ribeiro,[2,3] A. Eckmann,[4] R. Jalil,[5] B. D. Belle,[5] A. Mishchenko,[1] Y.-J. Kim,[1,6] R. V. Gorbachev,[1] T. Georgiou,[1] S. V. Morozov,[7] A. N. Grigorenko,[1] A. K. Geim,[5] C. Casiraghi,[4,8] A. H. Castro Neto,[2]*† K. S. Novoselov[1]

The isolation of various two-dimensional (2D) materials, and the possibility to combine them in vertical stacks, has created a new paradigm in materials science: heterostructures based on 2D crystals. Such a concept has already proven fruitful for a number of electronic applications in the area of ultrathin and flexible devices. Here, we expand the range of such structures to photoactive ones by using semiconducting transition metal dichalcogenides (TMDCs)/graphene stacks. Van Hove singularities in the electronic density of states of TMDC guarantees enhanced light-matter interactions, leading to enhanced photon absorption and electron-hole creation (which are collected in transparent graphene electrodes). This allows development of extremely efficient flexible photovoltaic devices with photoresponsivity above 0.1 ampere per watt (corresponding to an external quantum efficiency of above 30%).

The advent of graphene (*1*) and the subsequent discovery of its multitude of superior properties (*2*–*5*) has led to the identification of many other two-dimensional (2D) crystals (*6*) through both chemical modification of graphene and exfoliation of other layered compounds. This new area of research and progress in precise transfer of the crystals while maintaining their quality (*7*, *8*) has resulted in the emergence of a new class of materials: heterostructures based on 2D atomic crystals (*5*, *8*, *9*). More specifically, there is the possibility to create hybrid materials by stacking combinations of 2D crystals with differing properties. These structures are interesting from both fundamental and application points of view. It has, for instance, been shown that layering sheets of graphene and hexagonal boron nitride (hBN), molybdenum disulfide ($MoS_2$), or tungsten disulfide ($WS_2$) allows operation of tunneling transistors (*9*, *10*) and permitted the observation of phenomena such as Coulomb drag (*11*) and the fractional quantum Hall effect (*12*).

Many other crystals have been found to exfoliate to monolayer by both mechanical (*6*) and chemical methods (*13*). Transition metal dichalcogenides (TMDCs) are a group of layered materials that has attracted a lot of interest (*14*). They are structured such that each layer consists of three atomic planes: a triangular lattice of transition metal atoms sandwiched between two triangular lattices of chalcogen atoms (S, Se, or Te). There is strong covalent bonding between the atoms within each layer and predominantly weak van der Waals bonding between adjacent layers. Many of these materials—$NbSe_2$, $MoS_2$, $WS_2$, and $TaS_2$, to name a few—are structurally similar but have an array of electronic properties ranging from semiconducting (*15*) to metallic (*16*), from charge density waves to superconducting (*17*), depending on their exact composition, electronic density, geometry, and thickness (*18*).

Besides the traditional applications of TMDC films as solid-state lubricants and industrial surface protection (*19*, *20*), films of these materials have long been considered for photovoltaic devices, due to their large optical absorption, which is greater than $10^7$ $m^{-1}$ across the visible range, meaning that 95% of the light can be absorbed by a 300-nm film. A further advantage of $WS_2$ is its chemical stability (*21*, *22*) and band gaps in the visible part of the spectrum (*22*–*24*).

Previously, planar $WS_2$ (*21*) and $MoS_2$ (*22*) structures were studied for photovoltaic applications. However, efforts to extract photocurrent have been hampered by the need to create a p-n junction to separate the electron-hole (e-h) pairs created by incoming photons. Here, we show that, with the arrival of vertical 2D-crystal–based heterostructures, a beneficial combination of each material's properties emerges: TMDCs as good photoactive materials and graphene as a good transparent electrode. Using a Gr/TMDC/Gr stack (here, Gr stands for graphene) with appropriately

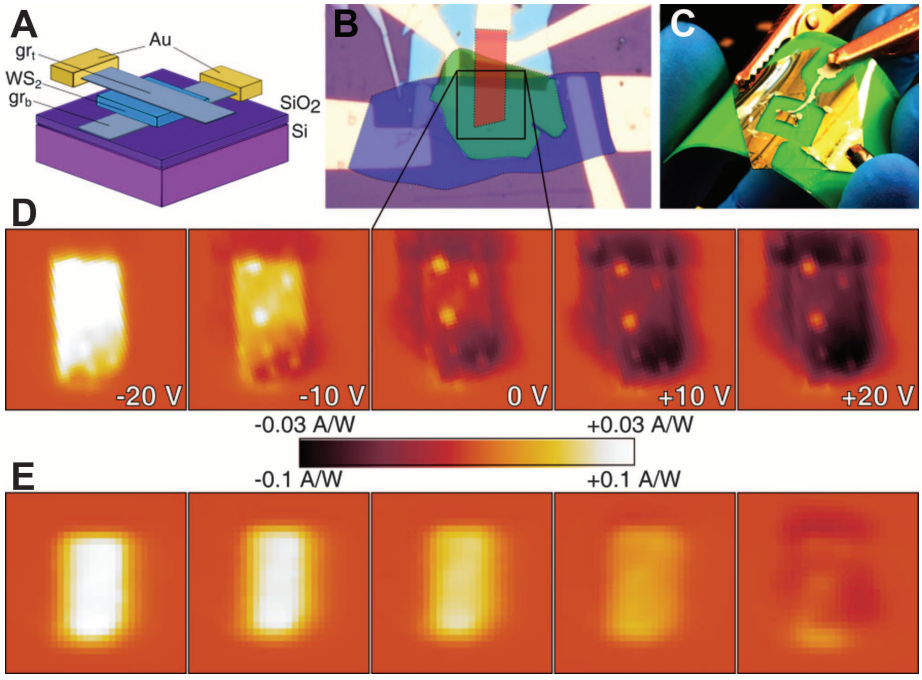


**Fig. 1. Device structure and photocurrent mapping.** (**A**) A schematic of the device with the principal layers shown. hBN is not shown. (**B**) An optical micrograph of one of our devices. The shading of the three constituent layers denotes the regions of the respective materials—top and bottom graphene electrodes are shown in red and blue, and $WS_2$ is shown in green. (**C**) A photograph of one of our flexible devices placed on an electroluminescent mat. (**D** and **E**) photocurrent maps taken before (D) and after (E) doping the top graphene layer with water vapor. A signal is only seen in the area where all three layers overlap. The two graphene layers were connected via a 1 kΩ resistor, on which the photocurrent was measured. No bias was applied, and for both (E) and (D), the maps were taken at gate voltages from −20 V to +20 V. The scale of the maps is given by their width, 20 μm.

[1]School of Physics and Astronomy, University of Manchester, Oxford Road, Manchester, M13 9PL, UK. [2]Graphene Research Centre, National University of Singapore, 6 Science Drive 2, Singapore 117546. [3]Departamento de Física and Centro de Física, Universidade do Minho, P-4710-057, Braga, Portugal. [4]School of Chemistry and Photon Science Institute, University of Manchester, Oxford Road, Manchester, M13 9PL, UK. [5]Manchester Centre for Mesoscience and Nanotechnology, University of Manchester, Oxford Road, Manchester, M13 9PL, UK. [6]Department of Chemistry, College of Natural Sciences, Seoul National University, Seoul, 151-747, Korea. [7]Institute for Microelectronics Technology, 142432 Chernogolovka, Russia. [8]Department of Physics, Freie University, Berlin, 14195, Germany.

*On leave from Department of Physics, Boston University, Boston, MA, USA.

†Corresponding author. E-mail: phycastr@nus.edu.sg

positioned Fermi levels and simply doping the two graphene layers differently (either by electrostatic gating or chemical methods) leads to a large photocurrent. The layered nature of our structures and exceptional mechanical strength of graphene and TMDC crystals (*25*, *26*) also allowed us to fabricate flexible devices. Without illumination, such devices act as tunneling transistors (*9*, *10*).

Although we concentrate the experimental data on the properties of Gr/$WS_2$/Gr heterostructures, our results are generic for a large class of systems where semiconducting TMDCs are the key element [see (*27*) for other examples of Gr/TMDC/Gr heterostructures].

Our devices comprise three principal elements—top and bottom graphene electrode layers (both micromechanically cleaved and chemical vapor deposition (CVD)–grown graphene were tested), sandwiching a photoactive TMDC layer (Fig. 1). In the fabrication procedure, the flakes were transferred with the "dry transfer" technique (in the case of micromechanically cleaved graphene) (*7*, *8*) with thorough annealing (*27*) at each stage to ensure minimal contamination between the layers (*28*) and low-level doping of the graphene layers. We also chose to use hBN as both a substrate and an encapsulating layer to achieve a higher doping homogeneity (*7*, *29*). Thus, the final structure of a typical device, on top of an oxidized silicon wafer or flexible polyethylene terephthalate (PET) film, was hBN/Gr/$WS_2$/Gr/hBN. In the case of nonflexible devices on Si/$SiO_2$, the doped silicon could be used as a back gate and $SiO_2$/hBN (typically 300 nm of $SiO_2$ and 20 nm of hBN) can be used as the gate dielectric. A series of such structures was produced where the thickness of the TMDC layer was varied from ~5 to 50 nm.

The current-voltage (*I-V*) characteristics of our samples strongly depended on illumination (Fig. 2A, left axis). Without illumination, the devices displayed strongly nonlinear *I-V* curves (Fig. 2A, right axis). Comparing the two sets of *I-V* curves, there is strong contrast to when they were illuminated: The resistance drops by more than three orders of magnitude, and the curves are linear around zero bias. At higher bias (~±0.2 V), the current saturates, as the number of available charge carriers in the photoactive region becomes limited.

The photocurrent generated in our devices was mapped by scanning photocurrent microscopy, where a laser spot was scanned over the sample, and the resultant photocurrent was displayed as a function of laser spot position. Photocurrent is generated only in the region where all three principal layers overlap (Fig. 1C). The origin of the photocurrent can be explained by examining the collective band diagram. In the idealized case, the structure is symmetric (Fig. 2B) and the electrons/holes generated in TMDC (by absorption of a photon with sufficient energy) have no preferred diffusion direction and, hence, no net photocurrent is measured. However, in the presence of a built-in electric field (Fig. 2C) across the TMDC [either due to a difference in the initial doping between the graphene sheets or by gating (*9*)], the e-h pairs are separated and a photocurrent measured.

Immediately after fabrication (which involves the annealing stage) in the undoped state, the devices showed a minimum in the integrated photocurrent close to zero gate voltage ($V_g$) (Fig. 1D). For any finite $V_g$ (either positive or negative), the photocurrent increased proportionally to $V_g$ but began to saturate at ~±20 V, again due to the finite number of generated charge carriers. We also intentionally doped the top graphene electrode in one of our nonencapsulated samples to become p-type by exposing it to high-concentration water vapor. The photocurrent (Fig. 1E) at zero gate voltage became finite (positive), and the response with gate voltage was shifted by ~20 V. The effect is also seen in Fig. 2A, where the intercept of the *I-V* curves is shifted due to movement of the chemical potential in graphene. Our devices also

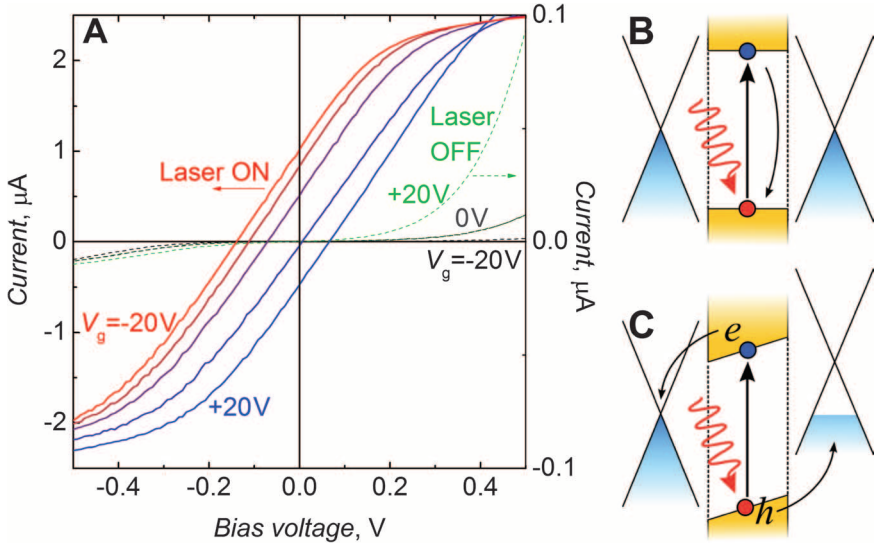


**Fig. 2. Gate-dependent *I-V* characteristics.** (**A**) (Left axis) *I-V* curves for a device on Si/$SiO_2$ taken under illumination at gate voltages from −20 (red) to +20 V (blue) in 10-V steps, after doping. The laser illumination energy was 2.54 eV and the power was 10 μW. The curves are linear at low bias but saturate at higher bias due to limited available charge carriers. (Right axis) *I-V* curves for the same device taken in the dark at gate voltages from −20 (black) to +20 V (green) in 20-V steps, after doping. (**B** and **C**) Schematic band diagram for Gr/$WS_2$/Gr heterostructure with (C) and without (B) a built-in electric field to separate the generated e-h pairs.

**Fig. 3. Electronic DoS for single-layer TMDCs.** (**A**) The DoS for monolayer TMDCs: $MoS_2$, $WS_2$, and $WSe_2$. Strong peaks are present in all three materials that lead to a strong light-matter interaction. (**B**) The JDoS with the same three TMDC materials.

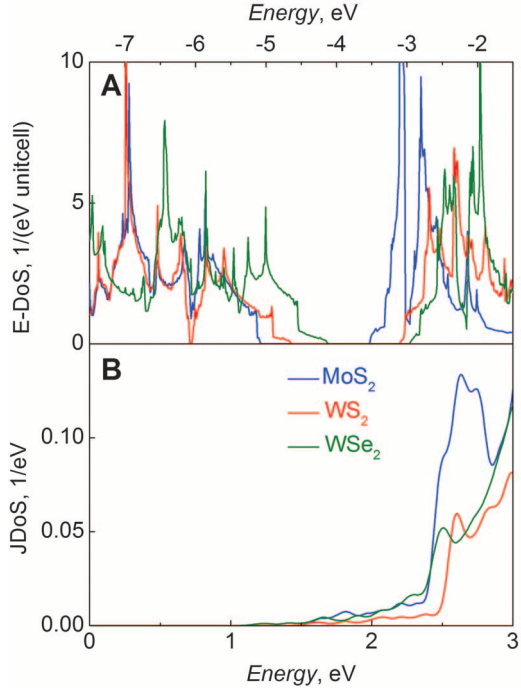

showed strong gate dependence without illumination, demonstrating transistor behavior. The on/off ratio (highest to lowest current modulation) of such tunneling transistors exceeds that of previously reported devices (*9*). Devices made from micromechanically cleaved and CVD graphene demonstrate very similar photovoltaic and transistor behavior, opening a way for scale-up.

The photocurrent observed in these devices is surprisingly strong for only a few atomic layers of TMDC, but this strong light-matter interaction can be understood from the nature of the electronic states in this material. Ab initio calculations (*27*) for the density of states (DoS) and the joint density of states (JDoS) of three single-layer semiconducting TMDCs ($WS_2$, $WSe_2$, and $MoS_2$) show strong peaks in the visible range (Fig. 3A) associated with Van Hove singularities in the DoS. This leads to enhanced light absorption and, importantly, this is a feature that is universal to TMDCs. These Van Hove singularities come from the nature of the electronic wave functions: Whereas the valence band is essentially composed of states coming from the d orbitals of the transition metal (TM), the conduction band is characterized by a linear superposition of d orbitals of the TM and p orbitals of the chalcogen atoms. The d orbitals have a localized nature with enhanced interaction effects. The p orbitals generate the σ bands, which in turn are responsible for the structural stability of these materials [analogous to what happens in graphene (*30*)]. The localized character of the electronic bands (that is, the large effective mass of the carriers) leads to the peaks—i.e., Van Hove singularities—in the DoS, which are responsible for the enhanced photoresponsivity of these materials from the nanoscopic down to atomic scale. A direct measure of the effect of the Van Hove singularities in the optical response of TMDC is given by the JDoS, defined as

$$JDOS(E) = \frac{1}{4\pi^3}\int d^3k\,\delta(E_{V,k} - E_{C,k} - E)$$

where $V$ and $C$ are the valence and conduction bands, respectively. The JDoS is a direct measure of the so-called joint critical points, that is, the Van Hove singularities in the Brillouin zone around which a photon of energy, $\hbar\omega = E_C - E_V$, is very effective in inducing electronic transitions over a relatively large region in momentum space. The large contribution to the transition probability for joint critical points gives rise to the structure observed in the frequency dependence of the optical properties of the TMDC. Thus, the photocurrent, $I(\omega)$, at some light frequency ω is proportional to $JDOS(\hbar\omega)$ (*31*). There is a sharp rise in the photo-absorption in the $JDOS(E)$ in the visible range of all TMDCs studied (Fig. 3B). To further confirm that our results are not dependent on the thickness of the TMDC, we calculated the DoS and JDoS for bulk (3D) semiconducting TMDCs (*27*). The peaks in the DoS and the sharp rise of the JDoS are comparable with the values found for a single layer in Fig. 3B and are consistent with the previous measurements on bulk $MoS_2$ (*32*). Hence, the strong light-matter interactions in semiconducting TMDCs are not a unique feature of the bulk material and can be extended to monolayers.

The effect discussed is similar, albeit with a different physical origin, to the strong Raman absorption in 1D semiconducting carbon nanotubes. In that case, the 1D nature of the material leads to $1/\sqrt{E}$ singularities in the DoS at the top (bottom) of the valence (conduction) bands, leading also to strong light-matter response (*33*).

We have also computed the work function, Φ, for the semiconducting TMDCs studied here. We find that the work functions vary considerably depending on the transition metal used (for monolayer, $\Phi_{WS_2} \sim 4.6$ eV, $\Phi_{WSe_2} \sim 4.3$ eV, and $\Phi_{MoS_2} \sim 5.1$ eV) and their thickness (for bulk, $\Phi_{WS_2} \sim 4.2$ eV, $\Phi_{WSe_2} \sim 3.9$ eV, and $\Phi_{MoS_2} \sim 4.5$ eV). Notice that as the work-function of graphene is comparable in magnitude ($\Phi_G \sim 4.5$ eV), it has been shown (*34*) that it has a very minimal effect on the band structure of TMDC, and the Dirac point of graphene stays within the gap, facilitating efficient extraction of both electrons and holes from TMDC.

We investigated in detail the performance of our prototype photovoltaic devices. An important parameter is the extrinsic quantum efficiency (EQE), defined as the ratio of the number of charge carriers generated to the number of incident photons. This can be expressed in terms of the photocurrent $I$, incident power per unit area $P$, and excitation wavelength λ by

$$EQE = \frac{hc}{e}\frac{I}{P\lambda}$$

where $h$ is the Planck constant, $c$ the speed of light in vacuum, and $e$ the electron charge. Using the relation for EQE, we calculate the efficiency (Fig. 4), where the data were collected for several wavelengths at zero bias and $V_g = -40$ V. The extrinsic quantum efficiency did not appear to be dependent on wavelength, as expected from the approximately constant optical absorption, over this range (*21*). It is likely that the decrease in quantum efficiency with increasing power is due to screening of the built-in electric field by the excited electrons in the conduction band of $WS_2$.

The already good performance and high EQE of our devices (ensured by the peculiar band structure of TMDC used) can be further improved by optimizing light absorption in the active layer. One possible way—the use of optical resonators (*35*)—is already partly realized in our devices on $SiO_2$, where light interference in $SiO_2$ layer (*36*, *37*) enhances the optical electric field in TMDC (this is one of the reasons for better performance of our devices on $SiO_2$ in comparison with those on flexible substrates). Another strategy is the use of plasmonic nanostructures (*38*–*40*) or metamaterials (*41*). To test the idea, we applied

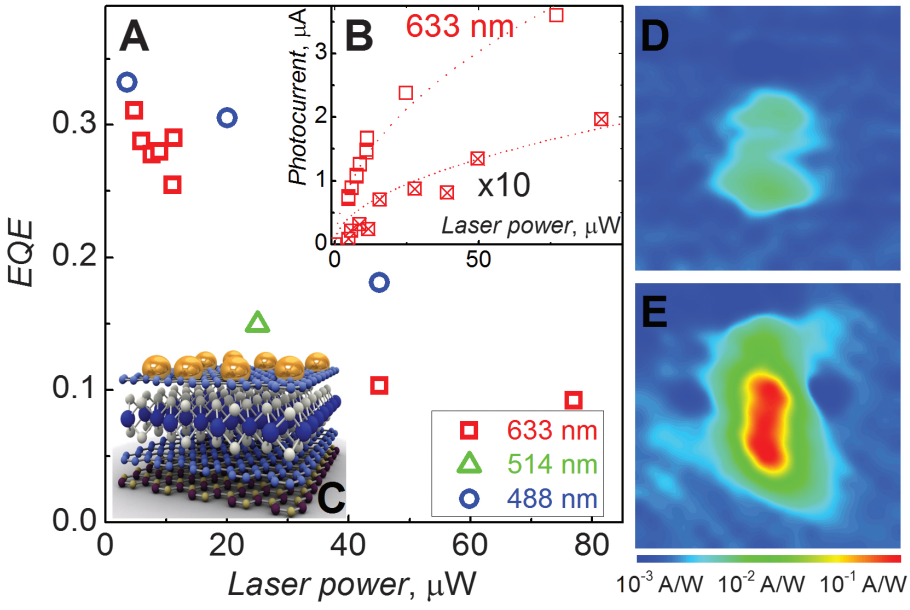


**Fig. 4. Quantum efficiency.** (**A**) The external quantum efficiency of the devices is the ratio of the number of measured e-h pairs to the number of incident photons. Due to the small variation in optical absorption across this wavelength range, the data for different wavelengths collapse onto a single curve. (**B**) Photocurrent measured with a 1.95-eV laser as a function of intensity; notice the sublinear dependence with laser power. This results in the largest quantum efficiency values at low intensities. Open symbols are for a device on $Si/SiO_2$ substrate, and crossed symbols are for a device on a flexible substrate. (**C**) Schematic representation of hBN/Gr/$MoS_2$/Gr (layers bottom to top) photovoltaic device with gold nanoparticles spattered on top of the top graphene layer for plasmonic enhancement of light absorption. (**D** and **E**) Photocurrent maps of one of our hBN/Gr/$MoS_2$/Gr devices taken before (D) and after (E) spattering of gold nanoparticles for plasmonic enhancement [illumination parameters: 633 nm, 10 μW; scan size, 14 μm by 14 μm; note the logarithmic scale chosen to represent the 10-fold increase in the photocurrent on (E)].

gold nanospheres (Fig. 4C) on top of one of our hBN/Gr/$MoS_2$/Gr heterostructures, which enhanced the optical field in the active layer and allowed for a 10-fold increase in the photocurrent, (Fig. 4, D and E) [see (*27*) for further details and other examples of the use of plasmonic nanostructures].

Atomically thin heterostructures of semiconducting TMDC present strong light-matter interactions that can lead to large photon absorption and photocurrent production. We are able to reach an extrinsic quantum efficiency of 30%, due to the localized character of the electronic wave functions in TMDCs that leads to large peaks in the DoS associated with van Hove singularities. The same devices demonstrate transistor behavior with on/off ratios exceeding those in previously reported devices. The use of various TMDCs, as well as their combinations, would allow one to create new transparent and flexible photonic and optoelectronic structures and devices with unique properties that surpass current technologies.

**References and Notes**


1. K. S. Novoselov *et al*., *Science* **306**, 666 (2004).
2. A. K. Geim, K. S. Novoselov, *Nat. Mater.* **6**, 183 (2007).
3. A. K. Geim, *Science* **324**, 1530 (2009).
4. A. K. Geim, *Rev. Mod. Phys.* **83**, 851 (2011).
5. K. S. Novoselov, *Rev. Mod. Phys.* **83**, 837 (2011).
6. K. S. Novoselov *et al*., *Proc. Natl. Acad. Sci. U.S.A.* **102**, 10451 (2005).
7. C. R. Dean *et al*., *Nat. Nanotechnol.* **5**, 722 (2010).
8. L. A. Ponomarenko *et al*., *Nat. Phys.* **7**, 958 (2011).
9. L. Britnell *et al*., *Science* **335**, 947 (2012).
10. T. Georgiou *et al*., *Nat. Nanotechnol.* **8**, 100 (2013).
11. R. V. Gorbachev *et al*., *Nat. Phys.* **8**, 896 (2012).
12. C. R. Dean *et al*., *Nat. Phys.* **7**, 693 (2011).
13. J. N. Coleman *et al*., *Science* **331**, 568 (2011).
14. Q. H. Wang, K. Kalantar-Zadeh, A. Kis, J. N. Coleman, M. S. Strano, *Nat. Nanotechnol.* **7**, 699 (2012).
15. L. F. Mattheiss, *Phys. Rev. B* **8**, 3719 (1973).
16. A. Ayari, E. Cobas, O. Ogundadegbe, M. S. Fuhrer, *J. Appl. Phys.* **101**, 014507 (2007).
17. A. H. Castro Neto, *Phys. Rev. Lett.* **86**, 4382 (2001).
18. A. Kumar, P. K. Ahluwalia, *Eur. Phys. J. B* **85**, 186 (2012).
19. M. R. Hilton, P. D. Fleischauer, *Surf. Coat. Tech.* **54-55**, 435 (1992).
20. S. R. Cohen *et al*., *Thin Solid Films* **324**, 190 (1998).
21. C. Ballif *et al*., *Appl. Phys. A Mat. Sci. Process.* **62**, 543 (1996).
22. E. Fortin, W. M. Sears, *J. Phys. Chem. Solids* **43**, 881 (1982).
23. K. K. Kam, B. A. Parkinson, *J. Phys. Chem.* **86**, 463 (1982).
24. H. Tributsch, H. Gerischer, C. Clemen, E. Bucher, *Phys. Chem. Chem. Phys.* **83**, 655 (1979).
25. C. Lee, X. D. Wei, J. W. Kysar, J. Hone, *Science* **321**, 385 (2008).
26. A. Castellanos-Gomez *et al*., *Nanoscale Res. Lett.* **7**, 233 (2012).
27. See supplementary materials on *Science* Online.
28. S. J. Haigh *et al*., *Nat. Mater.* **11**, 764 (2012).
29. A. S. Mayorov *et al*., *Nano Lett.* **11**, 2396 (2011).
30. A. H. Castro Neto, F. Guinea, N. M. R. Peres, K. S. Novoselov, A. K. Geim, *Rev. Mod. Phys.* **81**, 109 (2009).
31. B. E. A. Saleh, M. C. Teich, *Fundamentals of Photonics*. Wiley Series in Pure and Applied Optics (Wiley, New York, ed. 2, 2007).
32. V. V. Sobolev, V. V. Sobolev, *J. Appl. Spectrosc.* **61**, 532 (1994).
33. M. S. Dresselhaus *et al*., *Acc. Chem. Res.* **35**, 1070 (2002).
34. B. Sachs *et al*., Doping mechanisms in graphene-MoS2 hybrids; arXiv:1304.2236 (2013).
35. M. Furchi *et al*., *Nano Lett.* **12**, 2773 (2012).
36. P. Blake *et al*., *Appl. Phys. Lett.* **91**, 063124 (2007).
37. R. V. Gorbachev *et al*., *Small* **7**, 465 (2011).
38. S. M. Nie, S. R. Emory, *Science* **275**, 1102 (1997).
39. H. A. Atwater, A. Polman, *Nat. Mater.* **9**, 205 (2010).
40. T. J. Echtermeyer *et al*., *Nature Communications* **2**, 458 (2011).
41. O. Hess *et al*., *Nat. Mater.* **11**, 573 (2012).



**Acknowledgments:** This work was supported by the Royal Society, European Research Council, U.S. Army, EPSRC and European Science Foundation (ESF) under the EUROCORES Programme EuroGRAPHENE (GOSPEL). A.M. acknowledges support from the Swiss National Science Foundation. A.H.C.N. acknowledges support from the National Research Foundation (NRF) of Singapore through NRF-CRP award "Novel 2D materials with tailored properties: Beyond graphene" (R-144-000-295-281). Y.-J.K.'s work was supported by the Global Research Laboratory (GRL) Program (2011-0021972) of the Ministry of Education, Science and Technology, Korea. R.M.R. is thankful for the financial support of the Portuguese FCT under grant SFRH/BSAB/1249/2012.


**Supplementary Materials**

www.sciencemag.org/cgi/content/full/science.1235547/DC1
Materials and Methods
Supplementary Text
Figs. S1 to S9
References (*42*–*50*)


23 January 2013; accepted 18 April 2013
Published online 2 May 2013;
10.1126/science.1235547


# Redox Heterogeneity in Mid-Ocean Ridge Basalts as a Function of Mantle Source


**Elizabeth Cottrell[1]* and Katherine A. Kelley[2]**



**The oxidation state of Earth's upper mantle both influences and records mantle evolution, but systematic fine-scale variations in upper mantle oxidation state have not previously been recognized in mantle-derived lavas from mid-ocean ridges. Through a global survey of mid-ocean ridge basalt glasses, we show that mantle oxidation state varies systematically as a function of mantle source composition. Negative correlations between $Fe^{3+}/\Sigma Fe$ ratios and indices of mantle enrichment—such as $^{87}Sr/^{86}Sr$, $^{208}Pb/^{204}Pb$, Ba/La, and Nb/Zr ratios—reveal that enriched mantle is more reduced than depleted mantle. Because carbon may act to simultaneously reduce iron and generate melts that share geochemical traits with our reduced samples, we propose that carbon creates magmas at ridges that are reduced and enriched.**


The composition and geophysical properties of Earth's mantle have evolved in response to oxygen fugacity ($fO_2$), a measure of the chemical potential of oxygen in solid systems (*1*, *2*). Mantle-derived mid-ocean ridge basalts (MORBs) record $fO_2$ through the ratio of oxidized to total iron ($Fe^{3+}/\sum Fe$) (*3*), and, because MORBs also record geochemically distinct mantle reservoirs, the potential exists to discover the existence and evolution of heterogeneities in the oxidation state of the mantle. Two previous large ($n > 75$) global surveys of Fe oxidation states in MORB pillow glass (*4*, *5*) found no correlation between $Fe^{3+}/\sum Fe$ ratios and mantle source composition, establishing the paradigm that oceanic upper mantle oxidation state is relatively uniform, buffered, and not linked to plate tectonic–scale processes. Other work (*6*) has proposed that enriched mantle domains may be more oxidized than normal MORB. We determined high-precision (±0.005) $Fe^{3+}/\sum Fe$ ratios by micro–x-ray absorption near-edge structure (XANES) (*7*, *8*) and trace element concentrations on 19 glasses (from seven geographical locations) that have not experienced substantial fractionation [i.e., primitive MORB with MgO > 8.5 weight % (wt %)] or plume influence (*9*) (table S1). Additionally, a partially overlapping set of 22 glasses (from 10 geographical locations) from ridge segments without plume influence, irrespective of MgO content, previously published Sr ± Pb ± Nd isotope ratios (table S1). The primitive data set spans 50% of the global range in $Fe^{3+}/\sum Fe$ ratios, whereas the isotope data set spans the entire global range (fig. S1). Globally, the $Fe^{3+}/\sum Fe$ ratio in MORB negatively correlates with MgO concentration, whereby the $Fe^{3+}/\sum Fe$ ratio increases by ~0.03 as MgO decreases from 10 to 5 wt % (*8*) because $Fe^{2+}$ preferentially partitions into fractionating mafic phases. In order to account for the effect of fractionation, the $Fe^{3+}/\sum Fe$ ratios have been recalculated to an arbitrary reference value at MgO = 10 wt %, $Fe^{3+}/\sum Fe_{(10)}$, analogous to $Fe_2O_{3(8)}$ in (*4*, *8*). This correction is ~2% relative for the 19 primitive samples and is up to 11% (average of 7%) relative for the samples with isotopic data, but correlations between $Fe^{3+}/\sum Fe$ ratios, trace elements, and isotopes are also evident in the uncorrected data (*9*) (fig. S1).

The glasses form subparallel arrays in $^{208}Pb/^{204}Pb$-$^{206}Pb/^{204}Pb$ space as a function of $Fe^{3+}/\sum Fe$ ratio, with $^{208}Pb/^{204}Pb$ ratios increasing as


[1]National Museum of Natural History, Smithsonian Institution, Washington, DC 20560, USA. [2]Graduate School of Oceanography, University of Rhode Island, Narragansett, RI 02882, USA.

*Corresponding author. E-mail: cottrelle@si.edu

Science
AAAS

# Strong Light-Matter Interactions in Heterostructures of Atomically Thin Films

L. Britnell *et al.*

*Science* **340**, 1311 (2013);
DOI: 10.1126/science.1235547



*Science* (print ISSN 0036-8075; online ISSN 1095-9203) is published weekly, except the last week in December, by the American Association for the Advancement of Science, 1200 New York Avenue NW, Washington, DC 20005. 